

<https://doi.org/10.1038/s43247-025-02221-4>

High-latitude Southern Ocean eddy activity projected to evolve with anthropogenic climate change

Check for updates

Nathan Beech ^{1,2} ✉, Thomas Rackow ³, Tido Semmler ⁴ & Thomas Jung ^{1,5}

Ocean eddy activity in the high-latitude Southern Ocean is linked to critical drivers of the global climate, yet it is missing from effectively all projections of climate change due to computational costs. Using a high-resolution ocean model and cost-reducing simulation design, eddy activity in the high southern latitudes is revealed in detail, including three-dimensional spatial distribution and characteristics, unobstructed information beneath sea ice, and projections of future conditions after prolonged anthropogenic warming. The detected eddy activity is closely linked to large-scale circulation features like gyres and the Antarctic Slope Current. Eddy activity exhibits a strong seasonal cycle in which the presence of sea ice decreases the eddy population and increases the proportion of anticyclones. Anthropogenic warming is projected to shift eddy activity from the Antarctic Circumpolar Current poleward, intensify eddy activity along the Antarctic Slope Current, and reduce the seasonal cycle affecting eddy population and rotational direction.

The study of mesoscale ocean dynamics on a global scale has become drastically more accessible in recent decades through the development of satellite altimetry and high-resolution ocean models. Accordingly, the importance of mesoscale activity to global ocean and climate dynamics has become increasingly clear^{1–6}. Yet the effective range of altimetry-derived data and the eddy-resolving capabilities of the vast majority of model simulations do not reach the poles, where sea ice obscures the ocean surface and eddies can be smaller than the effective resolution of the altimetry products or model grids^{7–10}. These gaps in high-quality data have led to the omission of the high latitudes, and particularly the high-latitudes of the Southern Hemisphere, from many studies of ocean eddy activity. Yet the relevance of the polar regions to the global climate is widely accepted^{11–16}. Therefore, the missing polar mesoscale may be a serious shortcoming in the modern understanding of ocean dynamics. Now, new approaches to ocean modeling have been able to reduce the computational burden of investigating ocean eddy activity^{17,18}, presenting an opportunity to integrate the polar ocean mesoscale into the global understanding of ocean dynamics.

While the polar regions are challenging to research across scientific fields, it is undoubtable that the high-latitude Southern Ocean plays a critical role in global ocean circulation and climate. The seas surrounding the Antarctic continent host the formation sites of the Antarctic Bottom Water (AABW) occupying the deepest portions of the ocean and forming the lower

branch of global meridional overturning circulation (MOC)^{15,19,20}. The region hosts the southern part of the world's sea ice, steering Southern Hemisphere albedo²¹, transporting freshwater equatorward²², and representing a feedback mechanism for anthropogenic climate change²³. The Antarctic shelf waters, and particularly the Antarctic Slope Current (ASC), can shield the marine-terminating Antarctic glaciers and ice sheets from warmer waters, regulating freshwater flux from meltwater and again, representing a feedback mechanism to anthropogenic warming^{12,14}. Direct connections can be drawn between these globally impactful oceanic processes of the high southern latitudes and regional mesoscale activity; eddy activity introduces the precursors of AABW to the polar gyres^{24–26} and facilitates shoreward transport of warm mid-depth water onto the continental shelves where it can become denser and sink¹⁵. Seasonal ice melt may be hastened by eddy activity through the disturbance of insulating layers of cold meltwater below retreating ice^{27–29}. Mid-depth, cross-slope heat transport toward the Antarctic continent and ice shelves is attributed mainly to eddy activity, primarily through isopycnal eddy stirring^{30–32}, and eddies have been observed contributing to vertical heat transport in ice shelf cavities³³. While not an exhaustive list, these examples of mesoscale impacts on both high-latitude and global ocean circulation demonstrate the importance of high-latitude eddy activity both today and particularly in the context of anthropogenic warming.

¹Alfred Wegener Institute Helmholtz center for polar and marine research, Bremerhaven, Germany. ²Environmental Physics, Institute of Biogeochemistry and Pollutant Dynamics, Department of Environmental Systems Science, ETH Zürich, Zürich, Switzerland. ³European Center for Medium-range Weather Forecasts, Bonn, Germany. ⁴Met Éireann, the Irish Meteorological Service, Dublin, Ireland. ⁵Department of Physics and Electrical Engineering, University of Bremen, Bremen, Germany. ✉e-mail: nathan.beech@usys.ethz.ch

Although a comprehensive, pan-Antarctic description of the ocean mesoscale is absent from the literature, there is a patchwork of knowledge to be sourced from in-situ observations, remote sensing, and modeling research. Perhaps most notable, is the altimetry-derived sea surface height dataset of the seasonally ice-covered Southern Ocean, which is similar to the altimetry products typically used to study low-latitude eddy activity, but relies on measurements from sea ice leads³⁴. Eddy tracking has been applied to this dataset, but as the authors acknowledge, the dataset is too coarse to identify typical eddies in the region according to the local Rossby radius³⁵. Moreover, particularly in ice-covered regions, the peak of eddy activity is likely below the surface and beyond the range of sea surface height-based detection^{36–38} and substantial differences in eddy population and dynamics can exist between the mixed layer and deep ocean^{38–40}. In-situ observations of eddies also exist in the high latitudes^{41–47}, but are more common in the Arctic and, relative to satellite or model-based eddy tracking, the sample size and spatial coverage of observations is low. Finally, a limited range of modeling studies have been performed with resolutions sufficient to resolve eddy activity in the high southern latitudes. One such described the contribution of eddies to shoreward heat transport via scale decomposition³¹, but relied on just over a year of data and stopped short of a detailed description of mesoscale activity. Others rely on regional models to investigate various small-scale processes such as tidal or mesoscale contributions to circulation, but these can be limited in spatial scope⁴⁸, often stop short of describing the mesoscale itself^{49,50}, and can omit important external factors.

While limiting the scope and complexity of modeling studies can introduce caveats, these applications allow researchers to push the limits of what state-of-the-art modeling resources and infrastructure can facilitate. The alternative is to constrain simulations to lower-resolution configurations which lack high-latitude mesoscale flows, such as the Coupled Model Intercomparison Project (CMIP⁵¹). However, these simulations consistently perform poorly in the high latitudes^{52,53}, potentially confounding widely-referenced projections of global climate change. Moreover, it is unlikely that ocean resolutions even in the coming phases of CMIP will be sufficient to resolve high-latitude eddies. Thus, in order to investigate the impacts of mesoscale processes, cost-minimizing strategies are necessary.

The Finite volumE Sea-ice Ocean Model version 2 (FESOM2) is a post-CMIP6 model with multi-scale horizontal resolution capabilities, enabling the concentration of computational resources in focal regions within global simulations^{54–56}. This approach has now been demonstrated in multiple non-idealized use cases to be an effective approach to simulating mesoscale processes that would be computationally prohibitive with traditional model grids^{17,18,37}. In particular, Beech et al.¹⁸ employed FESOM2 to simulate the Southern Ocean in both a historical climatic state and a projected climate scenario following substantial anthropogenic warming with fully eddy-resolving conditions nearly until the Antarctic coast. This was accomplished by simulating the transient response to climate change with a lower-

resolution configuration of FESOM2 and branching off simulations with the regionally focused, high-resolution grid for shorter periods. This dataset has been demonstrated to accurately reproduce observed mesoscale activity, as well as the anticipated mesoscale response to climate change in the mid-latitude Southern Ocean¹⁸. Now, this dataset will be applied to the high southern latitudes to reveal the regional mesoscale structure and eddy characteristics, as well as their evolution in the context of anthropogenic climate change. In doing so, processes missing from most major global climate simulations can be identified and used to strengthen the existing oceanographic literature, interpret existing modeling studies, and inform future modeling efforts or observational campaigns.

Results

Regional eddy distribution

On the northern boundary of the study region, eddy activity from the Antarctic Circumpolar Current (ACC) is discernable by its eastward propagation, large eddy size and vorticity amplitude, and high eddy kinetic energy (EKE) (Figs. 1, 2a, 3a, d). Poleward of this, the path of the Antarctic Slope Current is host to near-circumpolar eddy activity with distinct westward propagation and interruptions only around the West-Antarctic Peninsula and the Iselin Bank of the Ross Sea (Fig. 1). Along the Antarctic continental shelf, bathymetric features that steer the mean flow meridionally intensify local mesoscale activity away from the coast (Fig. 1). In the Ross Sea, this occurs as the continental shelf at the Iselin Bank steers the ASC northward and in the eastern Weddell Sea, this occurs as the ASC interacts with the Gunnerus Ridge and Astrid Ridge. The Maud Rise also concentrates flow over its northern flank, elevating local eddy activity (Figs. 1, 2a, b, 4a). Eddy generation at the Maud rise is often linked to complex interactions with the distinct hydrography above the rise^{57–59}, but more generally, the bathymetric steering of mean flow is a source of eddy activity throughout the Southern Ocean^{18,60}. In the open ocean, where bathymetric features do not steer large-scale circulation, the Weddell Sea is the largest eddy-rich region poleward of the eastward-propagating ACC regime. Eddy trajectories tend to follow the closed contours of barotropic stream function associated with the circulation at the boundaries of the Ross and Weddell Gyres (Figs. 1, 3a). In both gyres, inflow at the northeast corners where ACC waters with anomalous densities can be introduced are sites of distinct poleward eddy propagation (Fig. 1). The presence of detected eddies is quite consistent with eddy kinetic energy from Reynolds decomposition (Fig. 2a), with the exception of the Ross Sea continental shelf, where relatively high EKE is either non-coherent or otherwise undetected (Figs. 1, 2a).

Following sustained anthropogenic climate change, the large, fast-moving, and eastward propagating ACC eddies in the north of the study region are projected to advance southward, generally occupying space that was previously eddy-poor, particularly the northern Bellingshausen and Amundsen seas and in the Australian-Antarctic Basin, north of the ASC

Fig. 1 | Regional distribution of ocean eddy activity south of 60°S. Eddy presence in 1951–1956 (left) and 2091–2096 (center) and the difference between the two periods (right) gridded on a 0.6° longitudinal spacing and a varying latitudinal step (see Methods) and smoothed by averaging grid centers within a 60 km radius. Black arrows are the mean eddy trajectories in a 2.5° latitude by 8° longitude grid overlaid for regions with a sample size greater than 60. Distances are exaggerated by a factor of 4 for visibility. The black contour is the 2200 m isobath.

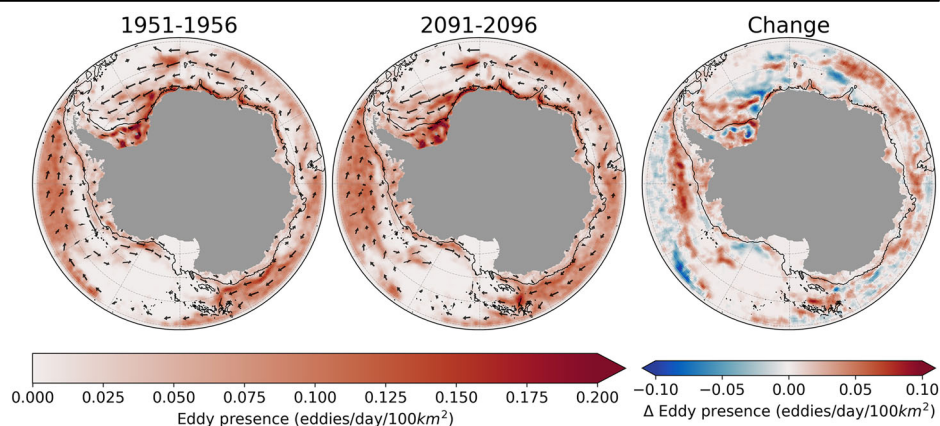
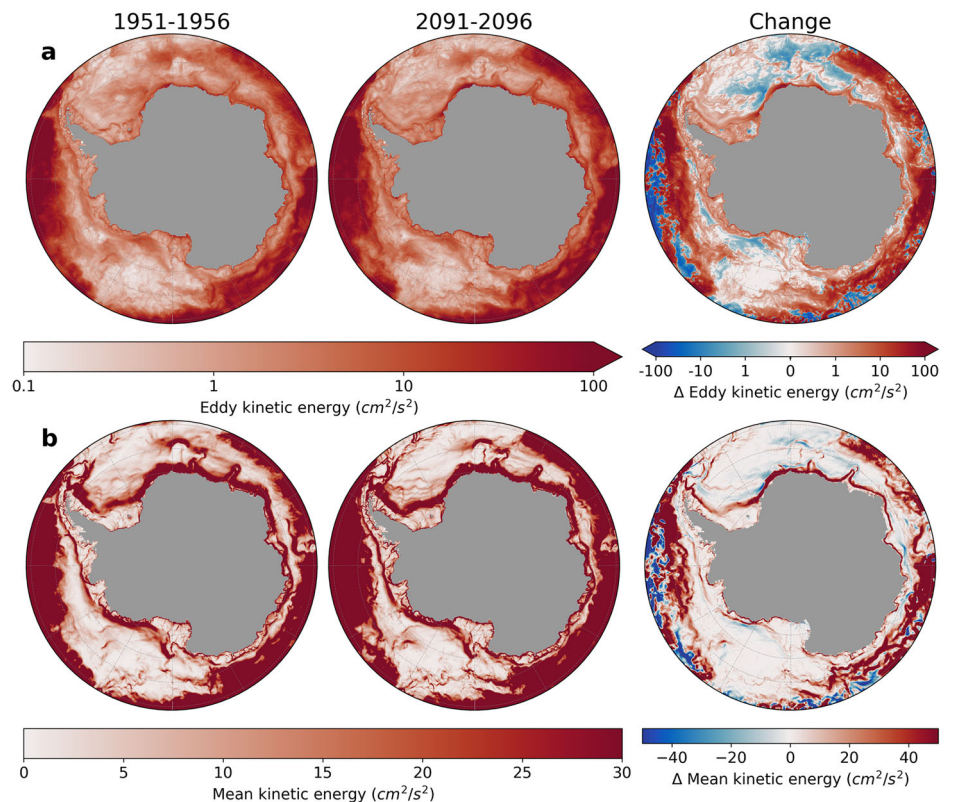


Fig. 2 | Simulated kinetic energy. **a** Mean eddy kinetic energy at 95 m depth. Note the logarithmic scales. **b** Mean kinetic energy and 95 m depth. The left column corresponds to the 1951–1956 period, the middle column corresponds to the 2091–2096 period, and the right column corresponds to the difference between the periods.



(Figs. 1, 3a, d). The intensification of the ACC and the poleward shift of its southern boundary has been relatively widely studied and attributed to trends in the Southern Annular Mode (SAM) and westerly winds^{61–63}, which are well represented in the model forcing data (Fig. 4c). Eddy activity is projected to intensify along the path of the ASC (Fig. 2a). Both baroclinic and barotropic generation mechanisms may contribute to the heightened eddy activity, as the mean flow of the ASC is projected to strengthen and the density gradient over the continental shelf break is projected to steepen (Figs. 2b, 4b). In the Weddell Sea, eddy activity is projected to advance westward into a former seasonal refuge for sea ice (Fig. 5a, b) where eddies were historically uncommon or absent (Fig. 1). Sea ice is known to have a dampening effect on eddy activity^{37,64} and this relationship will be explored further in the following paragraphs. In the Ross Sea, eddy activity associated with inflow at the northeast corner of the Ross Gyre intensifies and this is reflected by projections of the local density gradients (Figs. 2a, 4a, b). Eddy activity along the Ross Sea sector of the ASC appears constrained more closely to the continental shelf (Figs. 1, 2a), which is reflected by a narrowing or poleward shift of the mean flow in the region (Fig. 2b). The magnitude of the projected changes in eddy presence relative to the historical interannual range is high where the ACC enters formerly eddy-poor regions, where the ASC intensifies, and at the gyre inflows (Supplementary Fig. 1). It is lowest in regions historically occupied by ACC eddies and in the northern Weddell Gyre.

Regional eddy characteristics

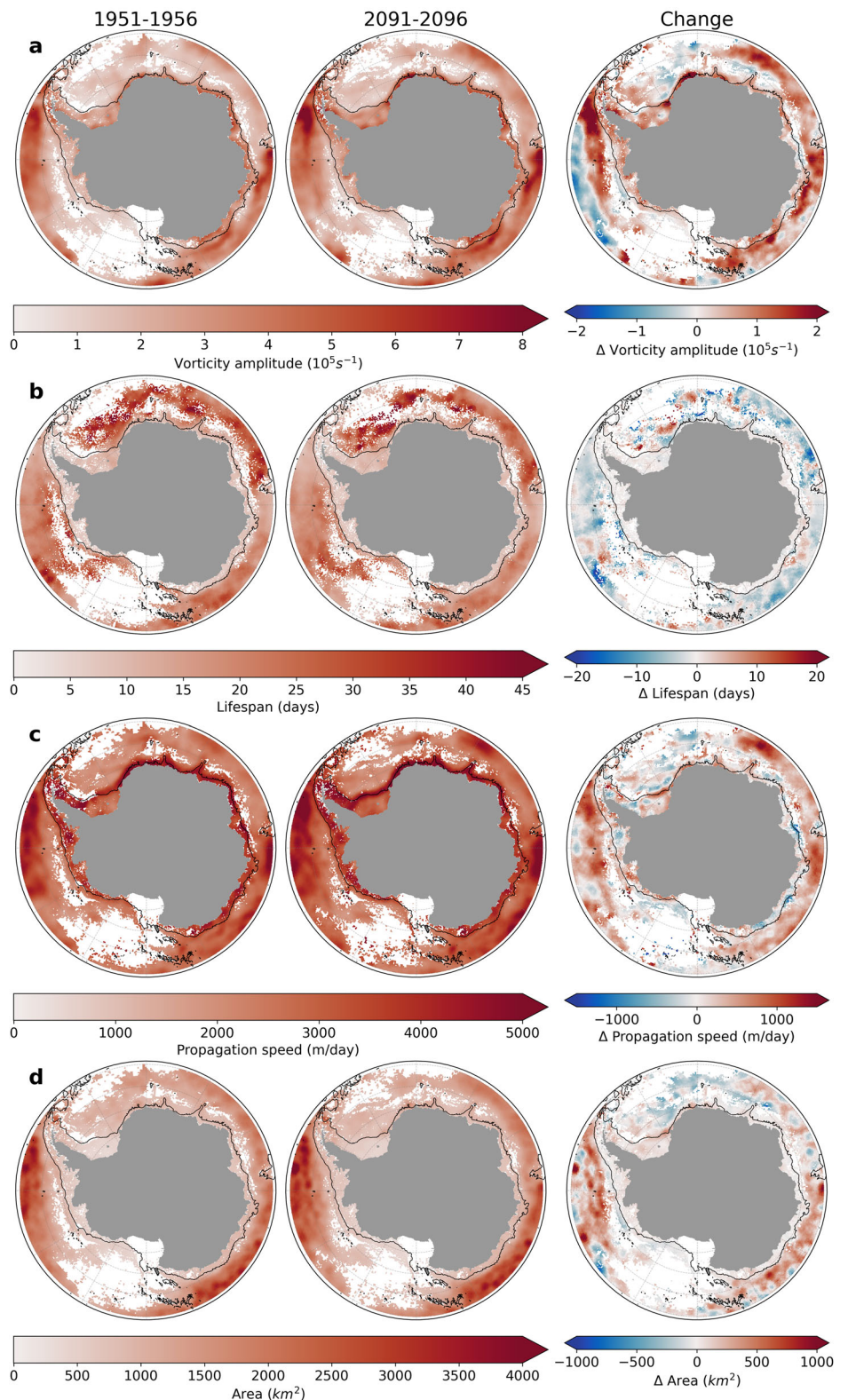
Eddy vorticity amplitude is high in regions with energetic largescale circulation, like the ACC and ASC, and is distributed similarly to EKE (Figs. 2, 3a). This is particularly apparent in the patterns of projected climate change impacts. Projections of vorticity amplitude reflect the aforementioned poleward shift of ACC eddy activity, intensification of ASC eddy activity, slight intensification of eddy activity at the gyre inflows, and eastward shift of eddy activity in the Weddell Gyre interior. The projected changes in vorticity amplitude are also some of the largest relative to the historical interannual range (Supplementary Fig. 2). Mean eddy lifespan tends to be

shortest in energetic regions of the ASC and ACC, and highest in the gyre interiors (Fig. 3b). Eddy propagation speed follows an inverse pattern, with high speeds along the path of the ASC and ACC and low speeds in the gyre interiors (Fig. 3c). This relationship indicates that movement with largescale background circulation is the primary driver of eddy propagation, but that highly energetic circulation features can also dissipate coherent eddies. Interestingly, eddy lifespan appears to surpass propagation speed in determining propagation distance, as the slow-moving gyre interiors also host farther-travelling eddies than the major currents (Fig. 1). Projected changes highlight the inverse patterns of propagation speed and lifespan; eddies become shorter-lived and faster-moving virtually throughout the study region, excluding parts of the Ross and Weddell gyres (Fig. 3a, b). While the opposing trends are clear, these changes tend to be small compared to historical interannual variability, particularly for lifespan which has a lower sample size than the other eddy characteristics (Supplementary Fig. 2). Eddy size varies strongly with latitude following the local baroclinic Rossby radius. The most substantial variation in eddy area along equal latitudes occurs in the ACC, where the effects of stratification and velocity shear are known to cause the baroclinic instability length scale to deviate from the local Rossby radius^{65,66}. After sustained warming, the major impact on eddy size in the study region is a poleward encroachment of large ACC eddies in the Amundsen and Bellingshausen Seas and the Australian-Antarctic Basin (Fig. 3d). In these regions, and in the southwest Weddell Sea, projected changes are large relative to historical interannual variability (Supplementary Fig. 2).

Seasonality and vertical distribution

The historical eddy population exhibits a seasonal peak in the austral summer (March–May) at approximately 95–100 m depth (Fig. 6a). The seasonal minimum population occurs in Austral winter (September–November), at the ocean surface (0–5 m), where and when the damping effects of sea ice are strongest (Fig. 4c). Both the cyclonic and anticyclonic eddy populations exhibit similar seasonal patterns and peaks as a function of depth (Fig. 6c, d), but anticyclones are more numerous than cyclones during

Fig. 3 | Regional characteristics of ocean eddy activity south of 60 °S. a Vorticity amplitude. **b** Lifespan. **c** Propagation speed. **d** Eddy area. Each variable is gridded with 0.6° longitudinal spacing and a varying latitudinal step (see Methods) and smoothed by averaging grid centers within a 100 km radius. The left column corresponds to the 1951–1956 period, the middle column corresponds to the 2091–2096 period, and the right column corresponds to the difference between the periods. The black contour is the 2200 m isobath.



Austral winter, reaching up to approximately 55% of the total population (Fig. 6b). The anticyclonic majority is concentrated at the surface and occurs just before the seasonal eddy minimum. In Austral summer, cyclones form the majority of eddies at depth and the cyclone/anticyclone populations at the surface are roughly equal. Mean eddy size peaks at approximately the same time as the population minimum and the anticyclonic majority (Fig. 7a, b) suggesting a filtering of smaller eddies by sea-ice damping, which

could favor the typically larger anticyclones. Both eddy types exhibit mean vorticity amplitude maxima around their population maxima (Fig. 7c, d), but interestingly, the cyclonic population includes a second vorticity maximum around the population minimum and the anticyclonic majority, which may further elucidate the selective sea-ice filtering.

After four degrees of warming, the eddy population rises substantially, with the largest increases occurring at the ocean surface in June and July

Fig. 4 | Selected simulated climatic variables.
a Vertically integrated horizontal barotropic stream function. **b** Mean potential density at 95–100 m depth. **c** Mean zonal wind speed. The left column corresponds to the 1951–1956 period, the middle column corresponds to the 2091–2096 period, and the right column corresponds to the difference between the periods.

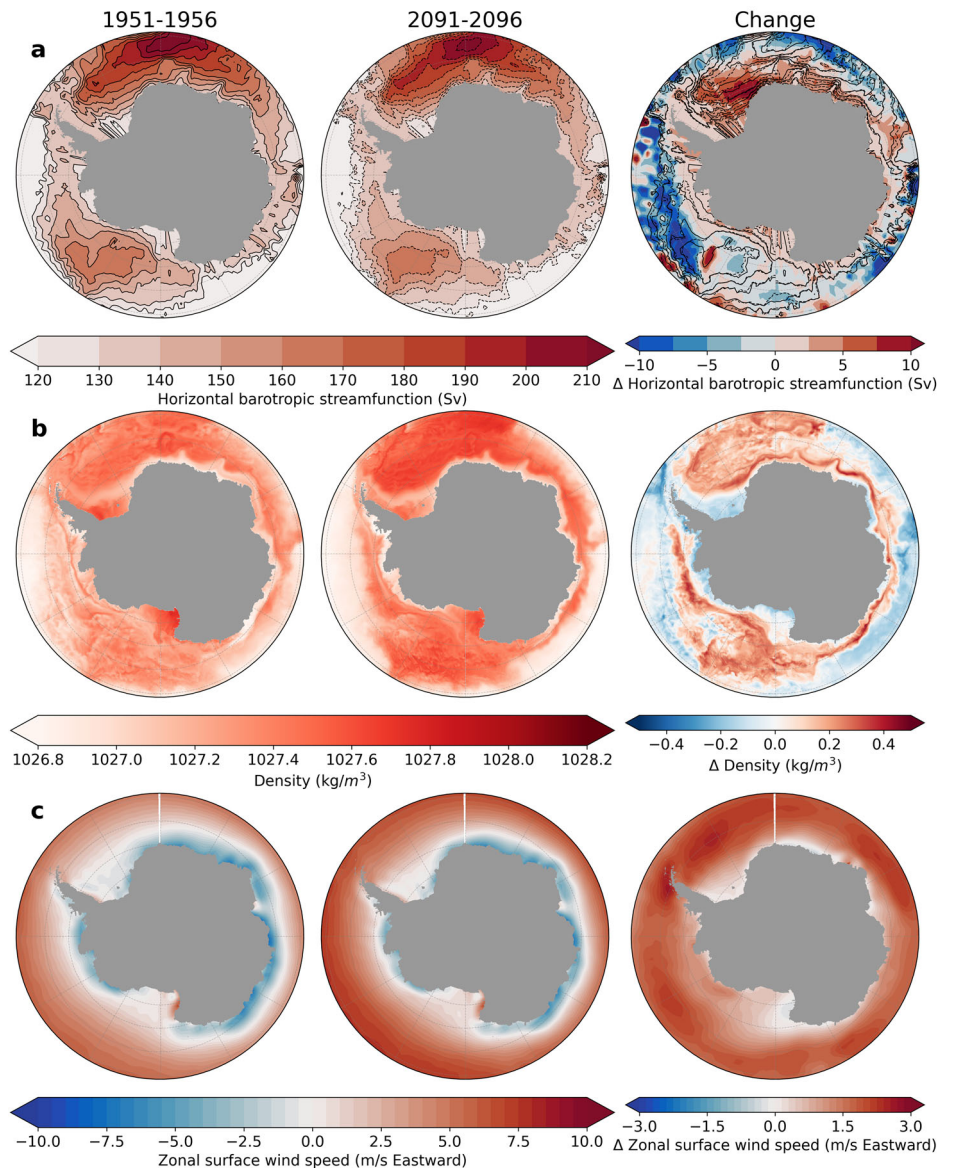


(Fig. 6a). The population peak remains at 95–100 m depth, but shifts from March/April to May, reflecting the extended period of low Southern Ocean sea ice (Fig. 4c). As in the historical period, both cyclonic and anticyclonic eddy populations exhibit similar seasonal and depth patterns (Fig. 6c, d), but vorticity regimes decline; the anticyclonic majority is weakened and concentrated closer to the surface, while the cyclonic majority at 180–200 m depth becomes weaker in Austral summer and extends further into Austral winter (Fig. 6b). Change in eddy size is weak at the historical peaks during the seasonal sea ice maximum and stronger at depth (Fig. 7a, b). The surface changes are consistent with a reduction in winter-season damping of small eddies by sea ice, enabling smaller eddies to survive and reduce the mean size (Fig. 3d). Mean vorticity amplitude rises with a similar pattern to population growth, but the winter-season cyclonic vorticity amplitude peak is greatly diminished, again, revealing a lesser role for sea ice (Fig. 7c, d).

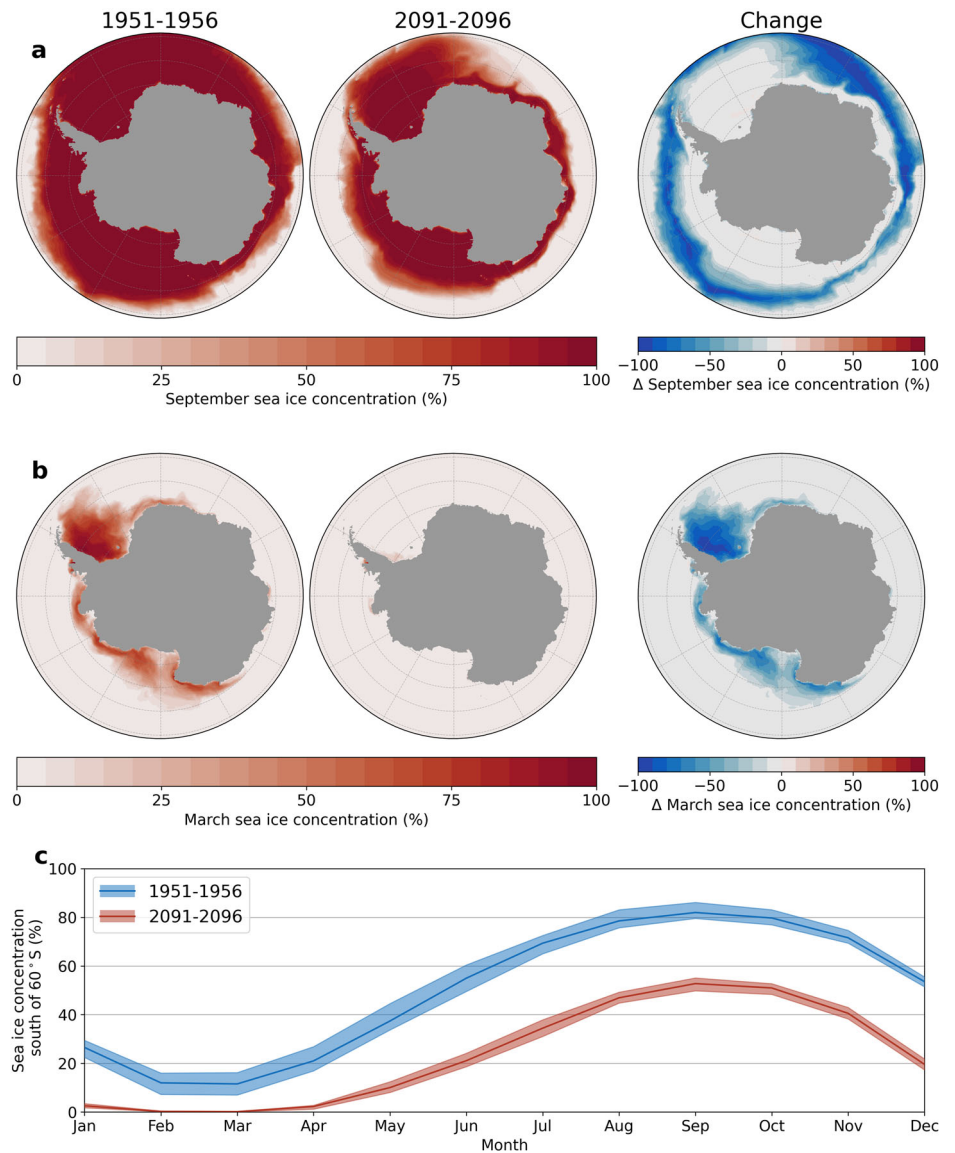
Discussion

The simulated regional distribution of eddy presence and characteristics is consistent with the largescale circulation features and eddy generation/dissipation mechanisms that dominate the study region. Similarly, the projected changes in eddy presence and characteristics can be linked to climate change impacts on these largescale drivers that are present in the

modeled dataset and, in most cases, anticipated in the context of climate change. For example, Southern Hemisphere westerlies are widely expected to shift south and intensify, altering the ACC and its eddy activity⁶¹. Antarctic meltwater is expected to strengthen the ASC⁶⁷, again providing more energy for eddy generation. Antarctic sea ice can be expected to decline substantially following prolonged climate change^{6,68}, reducing eddy-killing stress on the ocean surface. By linking the projected climate change impacts on eddy activity in the study region to more widely studied largescale circulation, the reliability of these projections is strengthened. As more reliable projections of high-latitude climate change become available, the results can be reinforced or reconsidered.

The impacts of the high-latitude eddies identified in this study on the wider climate are numerous; one is the introduction of Circumpolar Deepwater to the high latitudes, representing a critical step in the formation of AABW^{26,69}. The northeast corners of these gyres are regions where streamlines turn south and host most of the southward propagating eddies in the region (Fig. 1). This demonstrates the presence of an eddy-driven component of flow into the gyres, which is consistent with the published literature^{24,25}. Projections of climate change indicate an intensification of eddy activity at the Ross Gyre inflow and a decrease at the Northeast corner of the Weddell Gyre (Figs. 1, 2a). However, in the

Fig. 5 | Simulated sea ice seasonality and distribution. a September sea ice concentration. **b** March sea ice concentration. **c** Monthly sea ice concentration south of 60°S. In panels (a, b), the left column corresponds to the 1951–1956 period, the middle column corresponds to the 2091–2096 period, and the right column corresponds to the difference between the periods. In panel (c), dark red and blue lines represent the mean climatology and the shaded areas represent the range of monthly average sea ice concentration over the six-year periods.



Ross Gyre, these results may indicate an intensification of density gradients producing more, and more vigorous eddies, rather than more inflow (Figs. 3a, 4b). While in the Weddell Gyre, observations have identified two pathways of inflow from the lower latitudes²⁵, suggesting transport closer to the coast from the ASC may dominate AABW production. Ultimately, these results are insufficient to make definitive predictions regarding AABW production, but they indicate that research on AABW in the context of climate change must consider the role of eddies.

Once warm ACC waters reach the higher latitudes, eddy-driven cross-slope heat transport can bring heat toward the Antarctic ice sheets, threatening their vulnerable marine terminating flanks^{15,70}. Eddy activity is projected to intensify along the ASC path, particularly in the Weddell Sea (Figs. 1, 2a), which may intensify cross slope heat transport. To verify and elucidate this result, high spatial and temporal resolution temperature data, which was not saved from these simulations due to resource constraints, can be produced to enable direct quantification of shoreward heat transport in the context of climate change.

Sea ice is theorized to be responsible for both eddy generation and eddy killing in the mixed layer, with generation concentrated in the marginal ice zone and eddy killing in regions of denser pack ice^{35,37,39,64,71,72}. Pack ice and the marginal ice zone each have seasonal cycles that are not necessarily

consistent with one another^{73–75}, meaning the seasonal cycle of eddy activity must be interpreted as a cumulative response to these, as well as other seasonal processes. However, the spatial distribution of eddy activity remains concentrated around more typical eddy generation sites such as large-scale flows and fronts, as well as bathymetric features (Figs. 1, 2a), which is consistent with the lower latitudes^{8,36,60}. This indicates that eddy generation through sea ice processes plays a relatively minor role in these simulations, since the marginal ice zone could be expected to generate eddy activity in a more widespread area as it shifts spatially on a seasonal timescale. Alternatively, one may question the model’s ability to resolve eddies generated in the marginal ice zone, given that real sea ice floes can be smaller than the model grid scale, and the eddies generated may be sub-mesoscale, or smaller than the first baroclinic Rossby radius which these simulations were designed to resolve. Ultimately, further research is necessary to disentangle the various processes that contribute to the seasonal cycle of eddy activity identified in this study.

The modest majority of anticyclonic eddies during the winter months and near the ocean surface (Fig. 6b) is another indication of seasonal processes impacting eddy activity. The anticyclonic tendency of under-ice eddies has been observed in the Arctic, although with much greater anticyclonic dominance: up to 95% of the total population in some studies^{42,45–47}. The more modest majority of up to 55% anticyclones in the simulated high

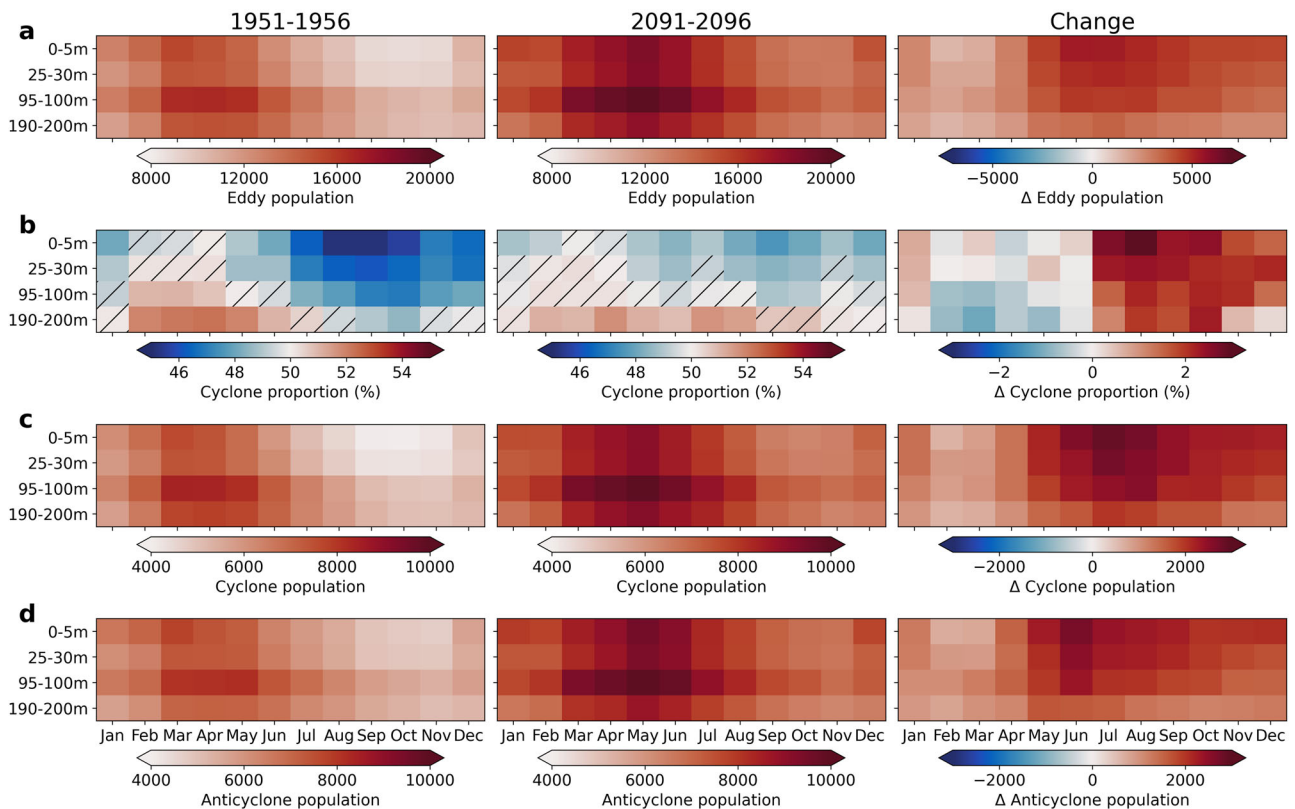


Fig. 6 | Eddy populations south of 60°S across depth and season. a Total eddy population. **b** Percentage of cyclones in the total eddy population. **c** Cyclonic eddy population. **d** Anticyclonic eddy population. Left column figures are of the 1951–1956 period, middle column figures are of the 2091–2096 period, right column

figures are the difference between the periods. The populations are defined as the sum of the monthly values over the entire six-year periods. Eddies that exist during multiple months are counted once in each month. Insignificant deviations from equal proportions at 95% confidence are hatched.

latitude Southern Ocean can be attributed to both regional and methodological differences; a larger proportion of the Arctic Ocean remains ice-covered through the summer months, allowing ice impacts to persist and compound. Furthermore, most studies of Arctic under-ice eddies use sea ice as an observational platform^{42,45–47} and tend to prefer thick multiyear ice in order to extend the lifespan of their observations⁷⁶, which may bias observations to regions where the impacts of sea ice are greatest. While these considerations do not repudiate observations of larger anticyclonic dominance in the Arctic eddy population, they do indicate that in regions of the Arctic with lower or more seasonal ice cover an anticyclonic eddy majority may be more modest and seasonal than existing studies would imply. In the context of climate change, the anticyclonic majority in both hemispheres can be expected to decline. Given the inverted thermal and haline anomalies typically associated with cyclones and anticyclones^{3,36,48}, this regime shift could have broader impacts on the polar regions.

While it is clear that sea ice impacts the eddy population, this study has not investigated the potential for eddies to modify the growth or decline of sea ice in turn. Relevant eddy impacts could include the disturbance of insulating meltwater layers^{27,28}, or more general vertical fluxes of heat and salinity that eddies are known to produce^{4,39,77,78}. The regions identified as eddy-rich in this study can serve as focal points to assess simple relationships and event-scale interactions between eddy activity and rates of seasonal ice growth and decline in both numerical or observational studies.

Conclusion

High-latitude Southern Ocean mesoscale activity has been revealed in a consistent, pan-Antarctic framework with unprecedented detail. Close links to currents, gyres, and bathymetry, as well as a sea ice-mediated seasonal cycle have been identified. The results can serve to unify the patchwork of existing knowledge from satellite altimetry, regional and idealized models, and in-situ observations. As anthropogenic climate change progresses, eddy

activity is projected to expand into formerly eddy-poor regions as ACC activity intrudes poleward and sea ice damping declines. Eddy activity along the path of the ASC and the northeast corner of the Ross Gyre is projected to intensify. Eddy characteristics are projected to shift in response to evolving largescale circulation patterns; eddy area increases where the ACC intrudes poleward, eddy lifespans decline and propagation speeds rise where background circulation intensifies, and eddy vorticity amplitude increases where eddy kinetic energy intensifies. Seasonal cycles in eddy population, characteristics, and vorticity direction are projected to weaken. These results carry implications for numerous climate-relevant processes including the production of AABW and heat transport toward Antarctic ice sheets. They demonstrate that eddy activity should be accounted for in dedicated studies of each of these processes, as well as high-quality projections of climate change in general.

Methods

Model simulations and data

The simulations analyzed in this study are described extensively in Beech et al.¹⁸. For the sake of completeness, a brief outline is included here. The model data was produced with the Finite volume Sea-ice Ocean Model version 2 (FESOM2⁵⁴) using a cost-reducing experiment design and a multi-resolution ocean grid with a regional focus on the Southern Ocean (Supplementary Fig. 7). FESOM2 is the successor of the Finite Element Sea-ice Ocean Model version 1.4 (FESOM1.4)⁷⁹ after numerous updates and improvements^{55,56} which are ongoing. The precise iteration of the model used in this study was FESOM2.5⁸⁰, which, among other things, implemented the ability to initialize sea ice variables from user-defined datasets; an important aspect of these experiments. The most notable feature of both FESOM1.4 and 2.5 is the unstructured horizontal ocean grid which employs a mesh of spherical triangles to enable variable horizontal resolutions throughout the model domain. The sea ice component is unique to FESOM,

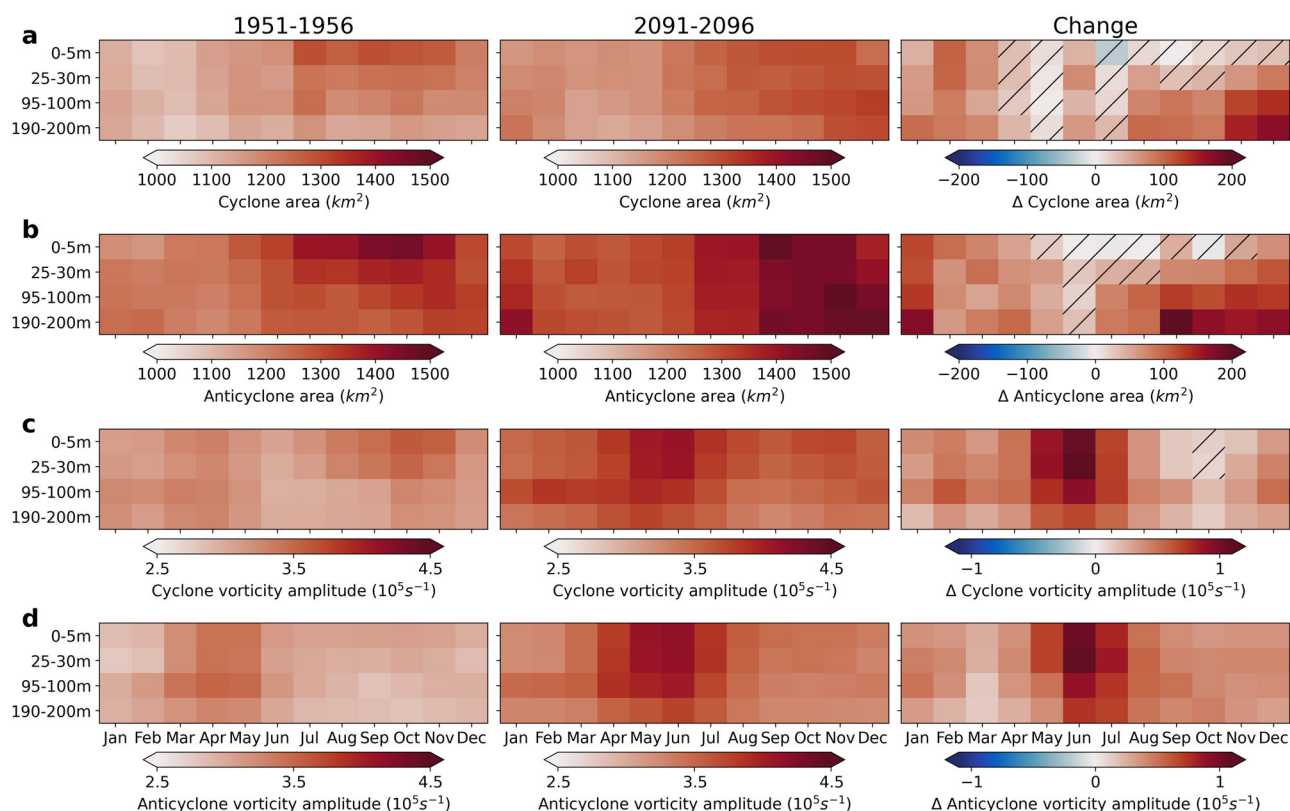


Fig. 7 | Eddy characteristics south of 60°S across depth and season. a Monthly mean area of cyclonic eddies. **b** Monthly mean area of anticyclonic eddies. **c** Monthly mean vorticity amplitude of cyclonic eddies. **d** Monthly mean vorticity amplitude of anticyclonic eddies. Left column figures are of the 1951–1956 period, middle column

figures are of the 2091–2096 period, right column figures are the differences between the periods. Average vorticity amplitude and area over each eddy's lifespan are calculated and grouped into months based on the middle date of the lifespan. Insignificant differences of means at 95% confidence are hatched.

the Finite Element Sea Ice Model, and employs elastic-viscous-plastic rheology⁸¹.

The simulations with FESOM2.5 consisted of four parts. The first was a transient, ocean-only simulation on a medium-resolution mesh stretching from 1851 to 2100, forced with atmospheric data taken from AWI-CM-1-1-MR's CMIP6 contribution⁸² to the historical⁵¹ and ScenarioMIP⁸³ simulation frameworks. During the projected period beginning in 2014, shared socioeconomic pathway (SSP) 3-7.0⁸⁴ is simulated, resulting in approximately 4 °C of mean global surface temperature rise as a result of anthropogenic climate change over the course of the simulations. This simulation was initialized from roughly preindustrial conditions after the 500-year spin-up period of AWI-CM-1-1-MR in the preindustrial control framework of CMIP6⁵¹. The ocean grid used in this simulation was the same one used by AWI-CM-1-1-MR during CMIP6, consisting of approximately 830,000 ocean surface nodes and horizontal resolutions ranging from 10–40 km in the Southern Ocean⁸². The three remaining simulations consisted of short time slices at various points during the progression of anthropogenic climate change, in which the model is reinitialized on a much higher-resolution, regionally focused mesh with the same atmospheric forcing as the medium-resolution transient simulation and initial ocean and sea ice conditions derived from the lower-resolution transient simulation. The high-resolution time slices began in 1950, 2015, and 2090, respectively, and were each run for 6 years. The first year of each simulation was discarded as a true spin-up, leaving 5 years of usable data. Later, the historical and projected period simulations were each extended by one year. The higher resolution mesh consists of 70 vertical layers and approximately 11 million nodes at the ocean surface, with a global resolution of approximately 25 km, gradually increasing to approximately 2.5 km in the Southern Ocean, the Agulhas current, and several narrow straits (Supplementary Fig. 7)⁸⁵. This configuration reaches eddy-resolving conditions in the ACC and the bulk of the Southern Hemisphere western boundary currents and maintains a global

resolution comparable to high-resolution CMIP6 models. Poleward of the ACC, the grid is still eddy-resolving, as measured by the local Rossby radius of deformation⁹, nearly to the Antarctic coast and only on the shelves does it become eddy-permitting or worse (Supplementary Fig. 7).

These simulations are made possible by a cost-reducing experiment design that necessarily also introduces caveats to the work. The high-resolution simulations are short and are not likely to reach a climatic equilibrium. Rather, the short simulations should reflect the climatic state of the much longer transient simulations from which they are initialized. Thus, the presence of mesoscale activity in the high-resolution simulations should not be expected to substantially change the model state. Rather, the simulated eddy activity can identify and characterize the mesoscale processes omitted from lower-resolution simulations. The short spin-up of the high-resolution simulations also makes them likely to drift. However, their length should reduce the amount by which they can deviate toward a new climatic state. Moreover, trends are not calculated within the simulations and the impacts of climate change are instead identified by comparing the mean states of the two climates. Therefore, the impacts of climate change simulated during the long transient simulation at lower resolution should be the dominant signal, rather than any effects of drift. It must be acknowledged that the lower-resolution transient simulation does not resolve local eddy activity, so the mesoscale activity identified in this study does not reflect the long-term impacts or feedback of this activity on the mean state of the climate.

Model evaluation

The model simulations with FESOM2 have been demonstrated to faithfully reproduce observed eddy activity in the mid-latitude Southern Ocean relative to observations, as well as the anticipated response of eddy activity to anthropogenic climate change¹⁸. The evaluation relative to observed conditions during the present day was performed using satellite altimetry data⁸⁶

during the 2016–2020 period. To assess the reliability of the projected climate impacts on eddy activity, the dataset was compared with an ensemble of more traditional, transient simulations from AWI-CM-1-1-MR in CMIP6^{17,18}. The ensemble agreement was used to identify regions of high- and low-confidence change and to distinguish between natural variability in eddy activity and the impacts of climate change after various degrees of warming. The results of the evaluation in Beech et al.¹⁸ were used to inform the analysis in this work; specifically, the limitation of the assessment of the impacts of climate change to the periods of 1951–1956 and 2091–2096. This will increase the signal-to-noise ratio of climate change to natural variability and help link the projected changes to anthropogenic impacts. Due to the limitations of the altimetry dataset at high latitudes and the ability of the CMIP6 dataset to resolve small eddies, the evaluation in Beech et al.¹⁸ is limited to the mid-latitude Southern Ocean and the ACC. Thus, an estimate of the natural variability of eddy activity in the high-latitude Southern Ocean must be made without a reference dataset. Moreover, the low sample size of the short simulations and the strong seasonal cycle and regional diversity of eddy activity in the region can invalidate the assumptions of traditional statistical tests such as a normally distributed dataset. As a transparent indication of the confidence of the results, the simulated historical ranges of annual eddy presence and characteristics are presented in Supplementary Figs. 1 and 2 along with the ratio of the projected climate change impacts over the historical range. Without asserting statistical significance, this measure can be used to identify lower or higher-confidence changes. As more extensive simulations become feasible, these results can be further scrutinized.

As a further validation of a sufficient signal-to-noise ratio of climate change to natural variability, the state of the dominant atmospheric mode of variability, the SAM, is presented in Supplementary Fig. 8. The SAM has substantial impacts on high-latitude Southern Ocean circulation and is one of the major mechanisms by which anthropogenic climate change affects the region⁶¹. Thus, it is important when assessing climate change impacts using short simulation lengths that the state of the SAM be consistent in each period. Using the Antarctic Oscillation Index (AOI⁶²), the state of the SAM is defined relative to conditions in each period respectively, as well as for the projected period relative to historic conditions (Supplementary Fig. 8). The AOI is relatively neutral relative to the conditions in each period respectively, whereas the projected AOI relative to historic conditions is substantially positive. This indicates that the modeled impacts of climate change on the SAM are large, whereas the other differences in the state of SAM which could be attributed to natural variability are comparably minor.

Explicit validation of the model performance in the study region is presented in Supplementary Figs. 3–6. Upper ocean temperature and salinity are compared to the Southern Ocean State Estimate (SOSE⁸⁸), and the World Ocean Atlas climatology (WOA⁸⁹) (Supplementary Figs. 3, 4). Simulated EKE at the ocean surface is compared with the SOSE, which at 1/6° horizontal resolution is referred to as eddy-permitting^{88,89}, as well as an altimetry-derived data product of geostrophic current anomalies from the seasonally-ice covered region of the Southern Ocean³⁴ (Supplementary Fig. 5a–c). Additionally, EKE at approximately 95 m depth is presented for SOSE and FESOM2 data (Supplementary Fig. 5d, f). Finally, the simulated sea ice concentration at the approximate seasonal maximum and minimum is presented and compared with satellite observations from the National Snow and Ice Data Center⁹⁰ (Supplementary Fig. S6).

Modeled upper ocean temperatures in the open ocean tend to be warmer than the WOA climatology and SOSE, with the largest differences occurring in the Australian sector of the Southern Ocean (Supplementary Figs. 3a, 4a). Temperatures over the continental shelf range from no bias to slightly colder. The simulated upper ocean tends to be fresher than both WOA and SOSE, with the largest differences occurring over the Weddell Sea and East Antarctic continental shelves and the Australian sector of the Southern Ocean (Supplementary Figs. 3b, 4b). EKE at the ocean surface (Supplementary Fig. 5a–c) is of comparable magnitude in all three datasets, although distinct features are difficult to discern, likely due to the effects of

wind and ice on surface velocity anomalies which are included in calculations of EKE using Reynolds decomposition. The observational product exhibits higher EKE than either simulated dataset over the large continental shelves in the Ross and Weddell Seas where both the SOSE and FESOM2 have low resolution relative to the local Rossby radius. Both the observational data product and the SOSE show broader regions of elevated EKE along the path of the ASC, potentially indicating a bias in the representation of the current in the FESOM2 simulations (Supplementary Fig. 5). Both the observational data product and the SOSE also have higher levels of EKE in the northern Ross Sea, demonstrating a bias regarding the shape of the Ross Gyre and the southern extent of the ACC in this region. At depth, where the effects of non-coherent EKE from wind and ice are lower, finer detail in eddy activity is apparent in each of the simulated datasets (Supplementary Fig. 5c,d), demonstrating the impacts of both surface processes and Reynolds decomposition. Simulated sea ice extent is generally lower than observed, with the exception of the northern Bellingshausen, Amundsen, and Ross seas during the seasonal maximum (Supplementary Fig. 6). During the seasonal minimum, key refugia of high-concentration sea ice, particularly in the southwest Weddell Sea, are present, but the continental shelf in East Antarctica becomes almost entirely sea-ice free. During the seasonal maximum, most of the study region is covered with pack ice, which the model captures well.

The magnitudes of temperature, salinity, and sea ice concentration biases in the FESOM2 simulations are comparable to those in the CMIP6 ensemble^{52,91,92} and the sea-ice bias tends to be negative, which is also consistent with most CMIP6 models⁹¹. While this is by no means a comprehensive evaluation of the overall model skill, the relevant ocean hydrography is reasonably represented relative to more traditional simulations from which a wealth of science has been produced. The sparsity of observational data in the Southern Ocean makes even the limited direct evaluation of simulated eddy activity relative to interpolated satellite measurements and an observationally constrained simulation in Supplementary Fig. 5 somewhat uncertain. Nonetheless, the high-resolution simulations with FESOM2 share key features of ocean eddy activity with each of the reference datasets, particularly as they relate to large-scale circulation features such as the ACC, ASC and gyres. Considering the substantial cost of tuning high-resolution models, the model skill demonstrated by the high-resolution FESOM2 simulations is already respectable. Moreover, what biases are present in the simulated climatic state do not interfere with a broadly accurate mesoscale field relative to the limited observations with which the model can be compared (Supplementary Fig. 5). Nonetheless, acknowledging the presence of biases can improve the interpretation of the model output as it relates to the real world.

Data processing

Daily velocity fields at selected vertical levels were first filtered and interpolated to a high-resolution, rectangular grid before eddy detection and tracking. The spatial filtering was performed using an implicit filter method described in⁹³, and a band pass filter between length scales of 10 and 100 km was chosen to isolate well-resolved eddies on the model grid (minimum radius twice the local grid spacing) and to help distinguish these features from larger background flow. Of course, since eddies are not always perfectly circular and filtering the velocity field may not fully remove the vorticity signature, smaller features may still be detected. Using linear interpolation, the smoothed data was transferred to a rectangular grid of 0.05° by 0.05° at the equator, with the latitudinal spacing reduced at higher latitudes to maintain approximately square grid cells. At high latitudes, the resulting rectangular grid is much higher resolution than the original grid to reduce any errors introduced through interpolation.

Eddy detection and tracking

Eddy detection based on the Okubo-Weiss parameter^{94,95} was performed using the python-based eddytools package after minor adjustments to accommodate interpolated FESOM2 data. The detection algorithm identifies continuous regions in which the Okubo-Weiss parameter (1) is below a

threshold, indicating that vorticity is dominant in the region.

$$w = s^2 + n^2 - \omega^2 \quad (1)$$

where w is the Okubo Weiss parameter, s is shear strain, n is normal strain, and ω is relative vorticity.

To be accepted as an eddy, regions must contain an interior minimum, in other words, have increasing vorticity dominance between the perimeter and interior, and fall within a range of acceptable sizes based on the number of grid cells contained within the eddy. The threshold for the Okubo Weiss parameter was defined as one tenth of the temporal mean of the spatial standard deviation over the entire study region during the historical period. This value was calculated separately for each depth, but kept constant during the historical and projected periods to maintain consistent criteria. The minimum number of grid cells to comprise an eddy was defined as 100, which, given the variability of the grid cell sizes, places the minimum radius for a circular detected feature at approximately 6.5 km at the southern end of the study region, and 15.6 km at the northern end. The maximum number of grid cells within an eddy was left arbitrarily large, meaning there was no upper limit defined for eddy size.

Detected eddies were tracked based on similarity of size, vorticity direction, vorticity amplitude, and separation. The minimum and maximum growth thresholds for size and vorticity amplitude were defined as 0.5 and 1.5, meaning an eddy can grow or shrink by a maximum of half of its previous size or vorticity amplitude per day. The maximum distance between two eddy detections was defined as 12 km per day, which roughly translates to an eddy propagating in a background flow of 0.14 m/s, a relatively high speed along the fastest-moving circulation feature in the focus region, the ASC⁹⁶. Finally, eddies with lifespans shorter than three days were removed, and eddies that dissipated after propagating less than 1 km per day from their point of genesis were removed.

The choices of parameters and thresholds in the detection and tracking steps were investigated thoroughly and the details of the effects are too numerous and minute to discuss entirely. Primarily, relaxing the thresholds for detection increases the number of detected eddies, but does not substantially change the spatial or seasonal distributions of the resulting eddy population. While some characteristics of the eddy population could be changed, such as lower average size given lower minimum thresholds, the spatial and seasonal patterns of these characteristics remained similar. Relaxing the thresholds during the tracking stage lowered the total number of tracked eddies and increased lifespans, suggesting that several eddies were combined into individual tracks, accurately or not. Other studies have performed more extensive evaluation of detection and tracking parameters through comparison with different algorithms and approximations of truth, but this work deserves its own dedicated study.

Eddy detection and tracking was performed at several depths in the upper ocean to produce a three-dimensional description of eddy activity that is necessarily absent from satellite and SSH-based detection methods. Across all depths, between 99,572 and 109,674 distinct eddies were tracked over their lifetimes during the 1951–1956 period, representing between 1,321,688 and 1,643,808 eddy-days of detections that were not discarded for failing to meet tracking thresholds described above. In the 2091–2096 period, between 127,434 and 143,092 eddies were tracked representing between 1,724,618 and 1,952,563 eddy detections across levels, excluded those that were discarded. For detailed population information across depths, see Figs. 6 and 7. Eddy populations and characteristics from each level are presented in Figs. 6 and 7. Spatial details are presented for the population peak at 95–100 m depth, but other levels produced only minor population differences from the peak depth and relatively consistent spatial distributions. Spatial figures for all depths are available in Supplementary Figs. 9–14.

Visualization

Eddy presence and characteristics in Figs. 1 and 3 were grouped spatially based on the position of the eddy center within an equal area grid with 0.6°

longitudinal spacing and variable latitudinal spacing which is reduced at higher latitudes to maintain approximately square grid cells. The binned spatial data is then smoothed by averaging bins within a radius of 60 km (Fig. 1) or 100 km (Fig. 3). For eddy characteristics in Fig. 3, grid cells that do not contain any eddy observations are not included in the smoothing process and remain blank, whereas for eddy presence in Fig. 1, zero is treated a valid value. The interannual historical range of eddy presence and characteristics in Supplementary Figs. 1 and 2 is the difference between the minimum and maximum annual value of each variable observed in any given simulated year of the historical simulations for each grid cell respectively. Due to the limited sample size after reducing the dataset to individual grid cells and the strong seasonality of the data, statistical significance tests are not performed on the regional projected changes.

In Figs. 6 and 7, eddies are grouped by month and characteristics or population sizes are calculated over the entire study region south of 60 °S. The use of the detected eddy population rather than Eulerian fields such as EKE ensures that the effects of wind and ice on the near surface ocean are not included in the assessment of eddy intensity as they are in Supplementary Fig. 5. It is important to acknowledge that many eddies are vertically coherent, meaning the same eddy may be identified in multiple layers in Figs. 6 and 7. However, many eddies are not coherent throughout the water column³⁸, particularly in the high latitudes, where the effects of sea ice and mixed layer dynamics play a major role³⁹. In Fig. 6b, the statistical significance of the proportion of either eddy type deviating from equality was calculated using a one-proportion z-test⁹⁷, while in Fig. 7 the difference between population means for each eddy characteristic between the two simulation periods was calculated using a two-tailed t-test assuming unequal variance and a normal distribution⁹⁸. For both Figs. 5 and 6, a threshold of $p < 0.05$ is used to indicate significance.

Data availability

Initial conditions used to initialize the FESOM2 simulations are publicly available at <https://doi.org/10.5281/zenodo.1497562799>. The SO3 mesh and other FESOM meshes are publicly available at <https://doi.org/10.5281/zenodo.14910006100>. Ocean velocity, temperature, and salinity data was acquired from the Southern Ocean State Estimate⁸⁸. Sea ice concentration data was retrieved from the NASA National Snow and Ice Data Center¹⁰¹. Ocean surface velocity anomaly data was acquired from SEANO³⁴. Ocean temperature and salinity data was acquired from the World Ocean Atlas¹⁰².

Code availability

The FESOM2 model code used to conduct these simulations is available at <https://doi.org/10.5281/zenodo.1047607280>. All code used to conduct the simulations with FESOM2 and perform the analysis is available at <https://doi.org/10.5281/zenodo.14975969103>.

Received: 17 January 2025; Accepted: 17 March 2025;

Published online: 26 March 2025

References

- Chassignet, E. P. et al. Impact of horizontal resolution on global ocean–sea ice model simulations based on the experimental protocols of the Ocean Model Intercomparison Project phase 2 (OMIP-2). *Geoscientific Model Dev.* **13**, 4595–4637 (2020).
- Chassignet, E. P. & Xu, X. On the Importance of High-Resolution in Large-Scale Ocean Models. *Adv. Atmos. Sci.* **38**, 1621–1634 (2021).
- Frenger, I., Gruber, N., Knutti, R. & Münnich, M. Imprint of Southern Ocean eddies on winds, clouds and rainfall. *Nat. Geosci.* **6**, 608–612 (2013).
- Gaube, P., Chelton, D. B., Samelson, R. M., Schlax, M. G. & O’Neill, L. W. Satellite Observations of Mesoscale Eddy-Induced Ekman Pumping. *J. Phys. Oceanogr.* **45**, 104–132 (2015).
- Griffies, S. M. et al. Impacts on Ocean Heat from Transient Mesoscale Eddies in a Hierarchy of Climate Models. *J. Clim.* **28**, 952–977 (2015).

6. Rackow, T. et al. Delayed Antarctic sea-ice decline in high-resolution climate change simulations. *Nat. Commun.* **13**, 637 (2022).
7. Amores, A., Jordà, G., Arsouze, T. & Le Sommer, J. Up to What Extent Can We Characterize Ocean Eddies Using Present-Day Gridded Altimetric Products?. *J. Geophys. Res.: Oceans* **123**, 7220–7236 (2018).
8. Ballarotta, M. et al. On the resolutions of ocean altimetry maps. *Ocean Sci.* **15**, 1091–1109 (2019).
9. Hallberg, R. Using a resolution function to regulate parameterizations of oceanic mesoscale eddy effects. *Ocean Model.* **72**, 92–103 (2013).
10. Sein, D. V. et al. Ocean Modeling on a Mesh With Resolution Following the Local Rossby Radius. *J. Adv. Modeling Earth Syst.* **9**, 2601–2614 (2017).
11. Bian, C. et al. Oceanic mesoscale eddies as crucial drivers of global marine heatwaves. *Nat. Commun.* **14**, 2970 (2023).
12. Bronselaer, B. et al. Change in future climate due to Antarctic meltwater. *Nature* **564**, 53–58 (2018).
13. Frey, D. I., Morozov, E. G. & Smirnova, D. A. Sea level anomalies affect the ocean circulation at abyssal depths. *Sci. Rep.* **13**, 20829 (2023).
14. Pauling, A. G., Smith, I. J., Langhorne, P. J. & Bitz, C. M. Time-Dependent Freshwater Input From Ice Shelves: Impacts on Antarctic Sea Ice and the Southern Ocean in an Earth System Model. *Geophys. Res. Lett.* **44**, 10,454–10,461 (2017).
15. Thompson, A. F., Heywood, K. J., Schmidtko, S. & Stewart, A. L. Eddy transport as a key component of the Antarctic overturning circulation. *Nat. Geosci.* **7**, 879–884 (2014).
16. van Westen, R. M. & Dijkstra, H. A. Ocean eddies strongly affect global mean sea-level projections. *Sci. Adv.* **7**, eabf1674 (2021).
17. Beech, N. et al. Long-term evolution of ocean eddy activity in a warming world. *Nat. Clim. Chang.* **12**, 910–917 (2022).
18. Beech, N., Rackow, T., Semmler, T. & Jung, T. Exploring the ocean mesoscale at reduced computational cost with FESOM 2.5: efficient modeling strategies applied to the Southern Ocean. *Geoscientific Model Dev.* **17**, 529–543 (2024).
19. Johnson, G. C. Quantifying Antarctic Bottom Water and North Atlantic Deep Water volumes. *J. Geophys. Res.: Oceans* **113**, C05027 (2008).
20. Orsi, A. H., Johnson, G. C. & Bullister, J. L. Circulation, mixing, and production of Antarctic Bottom Water. *Prog. Oceanogr.* **43**, 55–109 (1999).
21. Frey, W. R., Morrison, A. L., Kay, J. E., Guzman, R. & Chepfer, H. The Combined Influence of Observed Southern Ocean Clouds and Sea Ice on Top-of-Atmosphere Albedo. *J. Geophys. Res.: Atmospheres* **123**, 4461–4475 (2018).
22. Haumann, F. A., Gruber, N., Münnich, M., Frenger, I. & Kern, S. Sea-ice transport driving Southern Ocean salinity and its recent trends. *Nature* **537**, 89–92 (2016).
23. Colman, R. A comparison of climate feedbacks in general circulation models. *Clim. Dyn.* **20**, 865–873 (2003).
24. Roach, C. J. & Speer, K. Exchange of Water Between the Ross Gyre and ACC Assessed by Lagrangian Particle Tracking. *J. Geophys. Res.: Oceans* **124**, 4631–4643 (2019).
25. Ryan, S., Schröder, M., Huhn, O. & Timmermann, R. On the warm inflow at the eastern boundary of the Weddell Gyre. *Deep Sea Res. Part I: Oceanographic Res. Pap.* **107**, 70–81 (2016).
26. Schröder, M. & Fahrbach, E. On the structure and the transport of the eastern Weddell Gyre. *Deep Sea Res. Part II: Topical Stud. Oceanogr.* **46**, 501–527 (1999).
27. Gupta, M., Marshall, J., Song, H., Campin, J. -M. & Meneghello, G. Sea-Ice Melt Driven by Ice-Ocean Stresses on the Mesoscale. *J. Geophys. Res.: Oceans* **125**, e2020JC016404 (2020).
28. Horvat, C., Tziperman, E. & Campin, J. -M. Interaction of sea ice floe size, ocean eddies, and sea ice melting. *Geophys. Res. Lett.* **43**, 8083–8090 (2016).
29. Martínez-Moreno, J., Lique, C. & Talandier, C. Sea ice heterogeneity as a result of ocean eddy activity during the ice growth season.
30. Nøst, O. A. et al. Eddy overturning of the Antarctic Slope Front controls glacial melting in the Eastern Weddell Sea. *J. Geophys. Res.: Oceans* **116**, C11014 (2011).
31. Stewart, A. L., Klocker, A. & Menemenlis, D. Circum-Antarctic Shoreward Heat Transport Derived From an Eddy- and Tide-Resolving Simulation. *Geophys. Res. Lett.* **45**, 834–845 (2018).
32. Stewart, A. L. & Thompson, A. F. Eddy-mediated transport of warm Circumpolar Deep Water across the Antarctic Shelf Break. *Geophys. Res. Lett.* **42**, 432–440 (2015).
33. Friedrichs, D. M. et al. Observations of submesoscale eddy-driven heat transport at an ice shelf calving front. *Commun. Earth Environ.* **3**, 1–9 (2022).
34. Auger, M., Prandi, P. & Sallée, J. -B. Southern ocean sea level anomaly in the sea ice-covered sector from multimission satellite observations. *Sci. Data* **9**, 70 (2022).
35. Auger, M., Sallée, J. -B., Thompson, A. F., Pauthenet, E. & Prandi, P. Southern Ocean Ice-Covered Eddy Properties From Satellite Altimetry. *J. Geophys. Res.: Oceans* **128**, e2022JC019363 (2023).
36. Frenger, I., Münnich, M., Gruber, N. & Knutti, R. Southern Ocean eddy phenomenology. *J. Geophys. Res.: Oceans* **120**, 7413–7449 (2015).
37. Li, X. et al. Eddy activity in the Arctic Ocean projected to surge in a warming world. *Nat. Clim. Chang.* 1–7 <https://doi.org/10.1038/s41558-023-01908-w> (2024).
38. Petersen, M. R., Williams, S. J., Maltrud, M. E., Hecht, M. W. & Hamann, B. A three-dimensional eddy census of a high-resolution global ocean simulation. *J. Geophys. Res.: Oceans* **118**, 1759–1774 (2013).
39. Lu, K. et al. Lateral mixing across ice meltwater fronts of the Chukchi Sea shelf. *Geophys. Res. Lett.* **42**, 6754–6761 (2015).
40. Timmermans, M. -L., Cole, S. & Toole, J. Horizontal Density Structure and Restratification of the Arctic Ocean Surface Layer. <https://doi.org/10.1175/JPO-D-11-0125.1> (2012).
41. Cassianides, A., Lique, C. & Korosov, A. Ocean Eddy Signature on SAR-Derived Sea Ice Drift and Vorticity. *Geophys. Res. Lett.* **48**, e2020GL092066 (2021).
42. Manley, T. O. & Hunkins, K. Mesoscale eddies of the Arctic Ocean. *J. Geophys. Res.: Oceans* **90**, 4911–4930 (1985).
43. Morozov, E. G. et al. Mesoscale Variability of the Ocean in the Northern Part of the Weddell Sea. *Oceanology* **60**, 573–588 (2020).
44. Sallée, J. -B. et al. Subsurface floats in the Filchner Trough provide first direct under-ice tracks of eddies and circulation on shelf. *EGUosphere* 1–27. <https://doi.org/10.5194/egusphere-2023-2952> (2023).
45. Timmermans, M. -L., Toole, J., Proshutinsky, A., Krishfield, R. & Plueddemann, A. Eddies in the Canada Basin, Arctic Ocean, Observed from Ice-Tethered Profilers. *J. Phys. Oceanogr.* **38**, 133–145 (2008).
46. Zhao, M. et al. Characterizing the eddy field in the Arctic Ocean halocline. *J. Geophys. Res.: Oceans* **119**, 8800–8817 (2014).
47. Zhao, M., Timmermans, M. -L., Cole, S., Krishfield, R. & Toole, J. Evolution of the eddy field in the Arctic Ocean's Canada Basin, 2005–2015. *Geophys. Res. Lett.* **43**, 8106–8114 (2016).
48. Huot, P. -V., Kittel, C., Fichet, T., Jourdain, N. C. & Fettweis, X. Effects of ocean mesoscale eddies on atmosphere–sea ice–ocean interactions off Adélie Land, East Antarctica. *Clim. Dyn.* **59**, 41–60 (2022).
49. Graham, J. A., Dinniman, M. S. & Klinck, J. M. Impact of model resolution for on-shelf heat transport along the West Antarctic Peninsula. *J. Geophys. Res.: Oceans* **121**, 7880–7897 (2016).

50. Robertson, R. Baroclinic and barotropic tides in the Weddell Sea. *Antarctic Sci.* **17**, 461–474 (2005).
51. Eyring, V. et al. Overview of the Coupled Model Intercomparison Project Phase 6 (CMIP6) experimental design and organization. *Geoscientific Model Dev.* **9**, 1937–1958 (2016).
52. Luo, F., Ying, J., Liu, T. & Chen, D. Origins of Southern Ocean warm sea surface temperature bias in CMIP6 models. *npj Clim. Atmos. Sci.* **6**, 1–8 (2023).
53. Wang, C., Zhang, L., Lee, S. -K., Wu, L. & Mechoso, C. R. A global perspective on CMIP5 climate model biases. *Nat. Clim. Change* **4**, 201–205 (2014).
54. Danilov, S., Sidorenko, D., Wang, Q. & Jung, T. The Finite-volume Sea ice–Ocean Model (FESOM2). *Geoscientific Model Dev.* **10**, 765–789 (2017).
55. Scholz, P. et al. Assessment of the Finite-volume Sea ice–Ocean Model (FESOM2.0) – Part 1: Description of selected key model elements and comparison to its predecessor version. *Geoscientific Model Dev.* **12**, 4875–4899 (2019).
56. Scholz, P. et al. Assessment of the Finite-Volume Sea ice–Ocean Model (FESOM2.0) – Part 2: Partial bottom cells, embedded sea ice and vertical mixing library CVMix. *Geoscientific Model Dev.* **15**, 335–363 (2022).
57. Akitomo, K. Thermobaric deep convection, baroclinic instability, and their roles in vertical heat transport around Maud Rise in the Weddell Sea. *J. Geophys. Res.: Oceans* **111**, C09027 (2006).
58. Holland, D. M. Explaining the Weddell Polynya—a Large Ocean Eddy Shed at Maud Rise. *Science* **292**, 1697–1700 (2001).
59. Muench, R. D. et al. Maud Rise revisited. *J. Geophys. Res.: Oceans* **106**, 2423–2440 (2001).
60. Constantinou, N. C. & Hogg, A. McC. Eddy Saturation of the Southern Ocean: A Baroclinic Versus Barotropic Perspective. *Geophys. Res. Lett.* **46**, 12202–12212 (2019).
61. Marshall, G. J. Trends in the Southern Annular Mode from Observations and Reanalyses. *J. Clim.* **16**, 4134–4143 (2003).
62. Munday, D. R., Johnson, H. L. & Marshall, D. P. Eddy Saturation of Equilibrated Circumpolar Currents. *J. Phys. Oceanogr.* **43**, 507–532 (2013).
63. Yamazaki, K., Aoki, S., Katsumata, K., Hirano, D. & Nakayama, Y. Multidecadal poleward shift of the southern boundary of the Antarctic Circumpolar Current off East Antarctica. *Sci. Adv.* **7**, eabf8755 (2021).
64. Müller, V., et al. Variability of Eddy Kinetic Energy in the Eurasian Basin of the Arctic Ocean Inferred From a Model Simulation at 1-km Resolution. *J. Geophys. Res.: Oceans* **129**, e2023JC020139 (2024).
65. Tulloch, R., Marshall, J., Hill, C. & Smith, K. S. Scales, Growth Rates, and Spectral Fluxes of Baroclinic Instability in the Ocean. <https://doi.org/10.1175/2011JPO4404.1> (2011).
66. Vollmer, L. & Eden, C. A global map of meso-scale eddy diffusivities based on linear stability analysis. *Ocean Model.* **72**, 198–209 (2013).
67. Beadling, R. L. et al. Importance of the Antarctic Slope Current in the Southern Ocean Response to Ice Sheet Melt and Wind Stress Change. *J. Geophys. Res.: Oceans* **127**, (2022). e2021JC017608.
68. Purich, A. & Doddridge, E. W. Record low Antarctic sea ice coverage indicates a new sea ice state. *Commun. Earth Environ.* **4**, 1–9 (2023).
69. Orsi, A. H., Nowlin, W. D. & Whitworth, T. On the circulation and stratification of the Weddell Gyre. *Deep Sea Res. Part I: Oceanographic Res. Pap.* **40**, 169–203 (1993).
70. Pritchard, H. D. et al. Antarctic ice-sheet loss driven by basal melting of ice shelves. *Nature* **484**, 502–505 (2012).
71. Giddy, I., Swart, S., du Plessis, M., Thompson, A. F. & Nicholson, S. -A. Stirring of Sea-Ice Meltwater Enhances Submesoscale Fronts in the Southern Ocean. *J. Geophys. Res.: Oceans* **126**, e2020JC016814 (2021).
72. Meneghello, G. et al. Genesis and Decay of Mesoscale Baroclinic Eddies in the Seasonally Ice-Covered Interior Arctic Ocean. *J. Phys. Oceanogr.* **51**, 115–129 (2020).
73. Eyras, C. et al. Understanding the Seasonal Cycle of Antarctic Sea Ice Extent in the Context of Longer-Term Variability. *Rev. Geophysics* **57**, 1037–1064 (2019).
74. Gordon, A. L. Seasonality of Southern Ocean sea ice. *J. Geophys. Res.: Oceans* **86**, 4193–4197 (1981).
75. Vichi, M. An indicator of sea ice variability for the Antarctic marginal ice zone. *Cryosphere* **16**, 4087–4106 (2022).
76. Toole, J. M., Krishfield, R. A., Timmermans, M. -L. & Proshutinsky, A. The Ice-Tethered Profiler: Argo of the Arctic. *Oceanography* **24**, 126–135 (2011).
77. Mahadevan, A., Thomas, L. & Tandon, A. Comment on “Eddy/Wind Interactions Stimulate Extraordinary Mid-Ocean Plankton Blooms”. *Sci. (N. Y., N. Y.)* **320**, 448 (2008). author reply 448.
78. McGillicuddy, D. J. et al. Eddy/Wind Interactions Stimulate Extraordinary Mid-Ocean Plankton Blooms. *Science* **316**, 1021–1026 (2007).
79. Wang, Q. et al. The Finite Element Sea Ice–Ocean Model (FESOM) v.1.4: formulation of an ocean general circulation model. *Geoscientific Model Dev.* **7**, 663–693 (2014).
80. Danilov, S. et al. FESOM2.5_SO3. Zenodo <https://doi.org/10.5281/zenodo.10476072> (2024).
81. Danilov, S. et al. Finite-Element Sea Ice Model (FESIM), version 2. *Geoscientific Model Dev.* **8**, 1747–1761 (2015).
82. Semmler, T. et al. Simulations for CMIP6 With the AWI Climate Model AWI-CM-1-1. *J. Adv. Modeling Earth Syst.* **12**, e2019MS002009 (2020).
83. O’Neill, B. C. et al. The Scenario Model Intercomparison Project (ScenarioMIP) for CMIP6. *Geoscientific Model Dev.* **9**, 3461–3482 (2016).
84. Riahi, K. et al. The Shared Socioeconomic Pathways and their energy, land use, and greenhouse gas emissions implications: An overview. *Glob. Environ. Change* **42**, 153–168 (2017).
85. Danilov, S. On the Resolution of Triangular Meshes. *J. Adv. Modeling Earth Syst.* **14**, e2022MS003177 (2022).
86. Taburet, G. et al. DUACS DT2018: 25 years of reprocessed sea level altimetry products. *Ocean Sci.* **15**, 1207–1224 (2019).
87. Gong, D. & Wang, S. Definition of Antarctic Oscillation index. *Geophys. Res. Lett.* **26**, 459–462 (1999).
88. Mazloff, M. R., Heimbach, P. & Wunsch, C. An Eddy-Permitting Southern Ocean State Estimate. *J. Phys. Oceanogr.* **40**, 880–899 (2010).
89. Reagan, J. R. et al. World Ocean Atlas. (2023).
90. Meier, W. N., Fetterer, F., Windnagel, A. K. & Stewart, S. NOAA/NSIDC Climate Data Record of Passive Microwave Sea Ice Concentration, Version 4. <https://doi.org/10.7265/efmz-2t65> (2021).
91. Casagrande, F., Stachelski, L. & Souza, R. Assessment of Antarctic sea ice area and concentration in Coupled Model Intercomparison Project Phase 5 and Phase 6 models. *Int. J. Climatol.* **43**, 1–19 (2023).
92. Zhang, Q., Liu, B., Li, S. & Zhou, T. Understanding Models’ Global Sea Surface Temperature Bias in Mean State: From CMIP5 to CMIP6. *Geophys. Res. Lett.* **50**, e2022GL100888 (2023).
93. Danilov, S., Juricke, S., Nowak, K., Sidorenko, D. & Wang, Q. *Extracting Spatial Spectra Using Coarse-Graining Based on Implicit Filters*. <https://essopenarchive.org/users/523608/articles/656728-extracting-spatial-spectra-using-coarse-graining-based-on-implicit-filters?commit=52a394853a28aa985d8365d06cd26bcb5325f6b48> <https://doi.org/10.22541/essoar.169111691.14930425/v1> (2023).
94. Okubo, A. Horizontal dispersion of floatable particles in the vicinity of velocity singularities such as convergences. *Deep Sea Res. Oceanographic Abstr.* **17**, 445–454 (1970).
95. Weiss, J. The dynamics of enstrophy transfer in two-dimensional hydrodynamics. *Phys. D: Nonlinear Phenom.* **48**, 273–294 (1991).

96. Stewart, A. L., Klocker, A. & Menemenlis, D. Acceleration and Overturning of the Antarctic Slope Current by Winds, Eddies, and Tides. *J. Phys. Oceanogr.* **49**, 2043–2074 (2019).
97. Fleiss, J. L., Levin, B. & Paik, M. C. *Statistical Methods for Rates and Proportions*. (John Wiley & Sons, 2013).
98. Welch, B. L. The Generalization of ‘Student’s’ Problem when Several Different Population Variances are Involved. *Biometrika* **34**, 28–35 (1947).
99. Beech, N. Initial conditions used in FESOM2 simulations for Beech et al. (2025). Zenodo <https://doi.org/10.5281/zenodo.14975627> (2025).
100. Koldunov, N. V. & Harig, S. FESOM2 meshes: SO3. Zenodo <https://doi.org/10.5281/zenodo.14910006> (2025).
101. DiGirolamo, N., Parkinson, C. L., Cavalieri, D. J., Gloersen, P. & Zwally, H. J. Sea Ice Concentrations from Nimbus-7 SMMR and DMSP SSM/I-SSMIS Passive Microwave Data, Version 2. NASA National Snow and Ice Data Center Distributed Active Archive Center <https://doi.org/10.5067/MPYG15WAA4WX> (2022).
102. Reagan, J. R. et al. World Ocean Atlas 2023. NOAA National Centers for Environmental Information (2024).
103. Beech, N. n-beech/SO3_Antarctic_eddies: Re-release for zenodo. Zenodo <https://doi.org/10.5281/zenodo.14975969> (2025).

Acknowledgements

The authors thank Sergey Danilov and Kacper Nowak for their development of the implicit filter python package used during data preprocessing (https://github.com/FESOM/implicit_filter). The authors thank Nikolay Koldunov for the development of the pyfesom2 python package used during plotting (<https://github.com/FESOM/pyfesom2>). The authors thank Patrick Scholz for the development of the tripyview python used during plotting and the calculation of stream function (<https://github.com/FESOM/tripyview>). The authors thank Jan Klaus Rieck for the development of the eddytools python package used for eddy detection and tracking (<https://github.com/jk-rieck/eddytools>). T.J. was supported by the EERIE project (grant agreement ID 101081383) funded by the European Union. This research has been supported by the European Commission Horizon 2020 Framework Programme nextGEMS (grant no. 101003470). The work described in this paper has received funding from the Helmholtz Association through the project “Advanced Earth System Model Capacity” (project leader: Thomas Jung; support code: ZT-0003) in the frame of the initiative “Zukunftsthemen”. The content of the paper is the sole responsibility of the authors, and it does not represent the opinion of the Helmholtz Association, and the Helmholtz Association is not responsible for any use that might be made of information contained. This work used resources of the Deutsches Klimarechenzentrum (DKRZ) granted by its Scientific Steering Committee (WLA) under project ID 995.

Author contributions

N.B., T.R., T.S., and T.J. conceived of the study. N.B. performed the simulations and analyzed the data. N.B. drafted the manuscript. All authors contributed to the final version of the manuscript.

Funding

Open Access funding enabled and organized by Projekt DEAL.

Competing interests

The authors declare no competing interests.

Additional information

Supplementary information The online version contains supplementary material available at <https://doi.org/10.1038/s43247-025-02221-4>.

Correspondence and requests for materials should be addressed to Nathan Beech.

Peer review information *Communications Earth & Environment* thanks the anonymous reviewers for their contribution to the peer review of this work. Primary Handling Editor: Alice Drinkwater. A peer review file is available.

Reprints and permissions information is available at <http://www.nature.com/reprints>

Publisher’s note Springer Nature remains neutral with regard to jurisdictional claims in published maps and institutional affiliations.

Open Access This article is licensed under a Creative Commons Attribution 4.0 International License, which permits use, sharing, adaptation, distribution and reproduction in any medium or format, as long as you give appropriate credit to the original author(s) and the source, provide a link to the Creative Commons licence, and indicate if changes were made. The images or other third party material in this article are included in the article’s Creative Commons licence, unless indicated otherwise in a credit line to the material. If material is not included in the article’s Creative Commons licence and your intended use is not permitted by statutory regulation or exceeds the permitted use, you will need to obtain permission directly from the copyright holder. To view a copy of this licence, visit <http://creativecommons.org/licenses/by/4.0/>.

© The Author(s) 2025